locations near the bottom part of the cavity. The discrepancies could be due to the large conduction error in the temperature readings reported in the experiment. This is because the velocities in that region are small. In addition, the experiment shows that at $x = 1.0$, as the height along the z axis increases, the relative temperature correspondingly increases. This has also been observed in the computed results. The small discrepancies could be due to the assumption of the constant thermophysical properties.

The effect of grid density on the solution is shown in Fig. 2 by considering mesh sizes of $72 \times 24 \times 12$, $120 \times 40 \times 20$, and $168 \times 56 \times 28$ and by considering the converged values of the temperature at the location $(x, y, z) = (1.44, 0.80, 5.06)$. The various convergence curves begin at the initial ambient temperature of $\Theta = 0.5$, and as the grid is refined, the temperature approaches the value of 0.8, which corresponds to the experimental measurement. The $168 \times 56 \times 28$ grid gives the temperature value of approximately 0.79, with a 1.25% error. Further increase in the grid size beyond this size does not improve the value significantly.

Figure 3a shows the computed velocity vector field, and Fig. 3b shows the corresponding temperature contours on the middle y–z plane at $x = 1.00$, from which a recirculating fluid flow near the top of the cavity and a small secondary vortex just above the recirculating flow can be seen. This is caused by the entrapment of the pocket of fluid in the corner. As a temperature gradient is introduced into the flow, buoyancy effects will cause the flow of the fluid to be directed upward in the positive z direction. This buoyancy effect can be seen clearly in the vicinity of the hot wall, where the temperature T_h is imposed. It can be seen that the flowfield is divided into two distinct regions, the downward flow on the cooler side of the cavity and the upward flow on the hotter side. At about $y = 0.4$, it can be seen that the flow is virtually stagnant. The flow that is moving downward is driven mainly by inertia, whereas the flow that is moving upward is driven completely by buoyancy. The numerical results compare well with the flowfield contours based on the experimental data and the method has captured the relevant thermofluid physics of convective flows very well. Detailed results of the simulation can be found in Chong and Damodaran.[10]

Conclusions

In this study, the Godunov-projection method has been used to solve for the viscous incompressible flow with heat transfer in a lid-driven cavity. This projection method circumvents the problem arising from the lack of the time dependency of the density in the continuity equation. The energy equation is included with the momentum equations to solve the temperature field. The comparison between the numerical results and the experimental data shows good agreement thereby demonstrating the feasibility of using this algorithm for fluid flows with heat transfer. The maximum percentage error is about 10% and is mostly due to the large conduction error at the bottom of the cavity. The numerical simulation of the cavity flow reveals clearly the viscous effects at the wall boundaries and the shear force at the moving lid boundary. Grid convergence studies indicate that a grid size of $168 \times 56 \times 28$ and above is required to obtain numerical results that are within 1.25% of the experimental results. The present study has only focused on the feasibility of the numerical scheme to study steady-state convective flows. Future work will address the more general unsteady cavity flow in which perturbations will be imposed on the boundary conditions to simulate unsteady thermal and flow effects and the steady-state solutions obtained here will be used as the initial conditions to capture the evolving unsteady flowfields. The assumption of constant fluid properties will be discarded, and the governing equations will be modified to take into account the temperature dependency by way of coupling.

References

[1] Chorin, A. J., "A Numerical Method for Solving Incompressible Viscous Flow Problems," *Journal of Computational Physics*, Vol. 2, 1967, pp. 12–26.

[2] Gresho, P. M., "Some Current CFD Issues Relevant to the Incompressible Navier–Stokes Equations," *Computer Methods in Applied Mechanics and Engineering*, Vol. 87, 1991, pp. 201–252.

[3] Chorin, A. J., "Numerical Solution of the Navier–Stokes Equations," *Mathematics of Computations*, Vol. 22, Oct. 1968, pp. 745–762.

[4] Bell, J. B., Colella, P. and Howell, L. H., "An Efficient Second-Order Projection Method for Viscous Incompressible Flow," *Proceedings of the 10th AIAA Computational Fluid Dynamics Conference*, AIAA, Washington, DC, 1991, pp. 360–367.

[5] Godunov, S. K., "A Difference Scheme for Numerical Computation of Discontinuous Solution of Hydrodynamic Equations," *Math. Sbornik.*, Vol. 47, 1959, pp. 271–306.

[6] Pan, H., and Damodaran, M., "Parallel Computation of Viscous Incompressible Flows Using Godunov-Projection Method on Overlapping Grids," *International Journal of Numerical Methods in Fluids*, Vol. 39, No. 5, 2002, pp. 441–463.

[7] Koseff, J. R., and Street, R. L., "On End Wall Effects in a Lid-Driven Cavity Flow," *Journal Fluids Engineering*, Vol. 106, Dec. 1984, pp. 385–389.

[8] Prasad, A. K., and Koseff, J. R., "Combined Forced and Natural Convection Heat Transfer in a Deep Lid-Driven Cavity Flow," *International Journal of Heat and Fluid Flow*, Vol. 17, No. 5, 1996, pp. 460–467.

[9] Mansour, R. B., and Viskanta, R., "Shear-Opposed Mixed-Convection Flow and Heat Transfer in a Narrow, Vertical Cavity," *International Journal of Heat and Fluid Flow*, Vol. 15, No. 6, 1994, pp. 462–469.

[10] Chong, A. F., and Damodaran, M., "Parallel Computation of Viscous Incompressible Flows with Heat Transfer Using Second-Order Projection Methods," AIAA Paper 2001-2971, June 2001.

Buoyancy Effects on Three-Dimensional Convection Flow Adjacent to Backward-Facing Step

J. H. Nie[*] and B. F. Armaly[†]
University of Missouri–Rolla, Rolla, Missouri 65409

Introduction

SEPARATED and reattached flow occurs in many heat-exchanging devices, such as electronic and power generating equipment and dump combustors. A great deal of mixing of high- and low-energy fluid occurs in the separated and reattached flow regions, thus impacting significantly the heat transfer performance of these devices. Studies on separated flow have been conducted extensively during the past decades, and the backward-facing step geometry has received most of the attention.[1–3] The majority of published work dealt with the two-dimensional flow, and comparatively little is published about the three-dimensional nonisothermal case. Such knowledge is critical for optimizing the performance of physical heat-exchanging devices because they have mostly three-dimensional and nonisothermal flow. Forced convection results have been reported for a duct with an aspect ratio of 12 by Pepper and Carrington[4] and with an aspect ratio of 8 by Armaly et al.[5] To the authors' knowledge, the work of Iwai et al.[6] on the effects of duct inclination angle on heat transfer for a duct with aspect ratio of 16 and the work of Li and Armaly[7,8] on mixed convection in a duct with an aspect ratio of 8 are the only published three-dimensional results that incorporate the buoyancy force in the analysis for this simple geometry.

Received 1 September 2001; revision received 4 August 2002; accepted for publication 13 August 2002.

[*] Postdoctoral Fellow, Department of Mechanical and Aerospace Engineering and Engineering Mechanics.

[†] Curators' Professor, Department of Mechanical and Aerospace Engineering and Engineering Mechanics.

Problem Statement and Numerical Procedures

Three-dimensional, mixed convection flow adjacent to backward-facing step is numerically simulated, and a schematic of the calculation domain is shown in Fig. 1. The upstream height of the duct h is 0.01 m, the downstream height H is 0.02 m, and its width W is 0.08 m. This geometry provides a backward-facing step height S of 0.01 m, an expansion ratio $[ER = H/(H - S)]$ of 2, and an aspect ratio ($AR = W/S$) of 8. Because of the symmetry of the flow in the spanwise direction, the width of the computational domain is chosen as one-half of the actual width of the duct ($L = 0.04$ m). The streamwise length of the computational domain is chosen as 0.02 and 0.5 m upstream and downstream of the step, respectively, that is, $-2 \leq x/S \leq 50$. The origin of the coordinate system is located at the bottom corner of the step and sidewall, as shown in Fig. 1. By the use of the constant property assumption and the Boussinesq approximation, the steady three-dimensional Navier–Stokes and energy equations are solved, together with the continuity equation, using a finite volume method[9] to simulate the thermal and the flowfields (where T is temperature and u, v, and w are velocity components in coordinate directions x, y, and z). Li and Armaly[7] give details of the formulation. The physical properties are treated as constants and evaluated for air at the inlet temperature of $T_0 = 20°\mathrm{C}$, that is, density ρ is 1.205 kg/m^3, dynamics viscosity μ is 1.81×10^{-5} kg/m · s, specific heat $C_p = 1005$ J/kg · °C, thermal conductivity k is 0.0259 W/m · °C, and $\beta = 0.00341\ \mathrm{K}^{-1}$. Inlet flow at $x/S = -2$ is considered to be isothermal ($T_0 = 20°\mathrm{C}$), hydrodynamically steady, and fully developed.[10] A no-slip boundary condition (zero velocities) is applied to all of the wall surfaces. A thermally adiabatic boundary condition is specified at all of the walls with the exception of the downstream stepped wall, which is supplied with a uniform heat flux q_w. The uniform heat flux boundary condition at the downstream stepped wall is varied to investigate the effects of buoyancy [i.e., the Grashof number ($Gr = \rho^2 g\beta q_w S^4/\mu^2 k$, where g is gravitational acceleration)], on the flow and heat transfer. A symmetry condition is imposed at the center width of the duct, and a fully developed condition is imposed at the exit section ($x/S = 50$).

A detailed description of the numerical scheme, grid distribution, grid independence tests, and convergence criteria that were used in this simulation can be found in Ref. 8. All calculations were performed on a Gateway PIII 933 desktop computer, with one iteration requiring approximately 14.98 s when the total number of grid points was about 1.5×10^5. The laser Doppler velocimeter measurements[11] in the simulated geometry at Reynolds numbers of $Re = 98.5$ and 343 ($Re = 2\rho u_0 h/\mu$, where u_0 is the average inlet velocity) were used for validating the developed computer code. A very good comparison between measured and predicted x_u lines, where the streamwise velocity component is zero on a plane adjacent to the heated wall ($y/S = 0.01$), was obtained, as shown in Fig. 2. This provided code validation for exploring the effects of buoyancy force on the flow and heat transfer characteristics in this geometry. A Reynolds number of 200 was selected for this study to cover a range of buoyancy force between $0 \leq Gr/Re^2 \leq 0.1$, while maintaining laminar flow conditions in the duct.

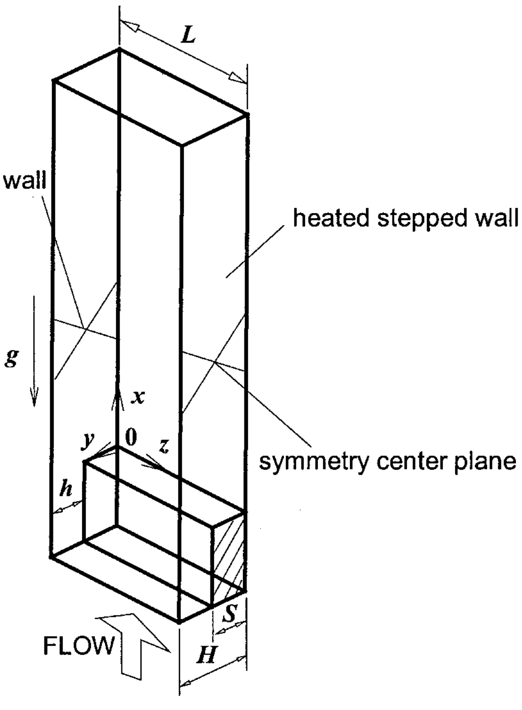

Fig. 1 Schematic of the computation domain.

Table 1 Starting locations (x, y, z) of the streamlines

Number	$Gr = 0$	$Gr = 1000$	$Gr = 4000$
1	(−2, 1.834, 0.040)	(−2, 1.825, 0.067)	(−2, 1.920, 0.088)
2	(−2, 1.813, 0.047)	(−2, 1.819, 0.068)	(−2, 1.600, 0.010)
3	(−2, 1.848, 0.042)	(−2, 1.799, 0.044)	(−2, 1.936, 0.086)

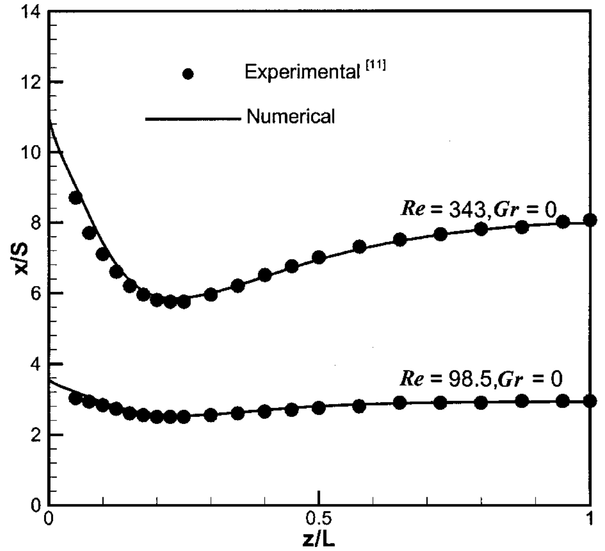

Fig. 2 Comparison of measured and predicted x_u lines on $y/S = 0.01$.

Results and Discussions

The present work is an extension to the one reported by Armaly et al.[5] dealing with forced convection in the same geometry. This study is focused on examining the effects of buoyancy on the flow and heat transfer characteristics. Figures 3 and 4 demonstrate the effects of the Grashof number on the flow patterns with the aid of streamlines. The streamlines in Fig. 3 illustrate the various flowpaths followed by massless particles that start at the inlet plane close to the sidewall. Different streamlines are selected for each of Figs. 3a–3c to capture the flow features for various Grashof numbers. The starting points for these streamlines at the inlet plane are listed in Table 1. For forced convection flow ($Gr = 0$) in Fig. 3a, the streamlines capture the swirling flow that develops inside the primary recirculation flow region and the reverse flow that develops adjacent to the sidewall. In Fig. 3a, the primary recirculation region can be seen clearly as captured by interpolating between limiting streamlines. The limiting streamlines that are shown in Fig. 4 at $y/S = 0.01$ are used to identify the outer boundary of the primary recirculation flow region, x_b, and that is presented as a dashed line in Fig. 3. This boundary, x_b, is determined by the criterion that the streamlines on both sides of this boundary line move in opposite directions: The streamlines upstream from this line flow upstream toward the step, and the streamlines downstream from this line flow downstream and away from the step. This boundary line x_b is different from the zero-mean streamwise velocity that is presented in Fig. 2, line x_u, due to the strong spanwise velocity component that develops close to the step in this three-dimensional flow. These two

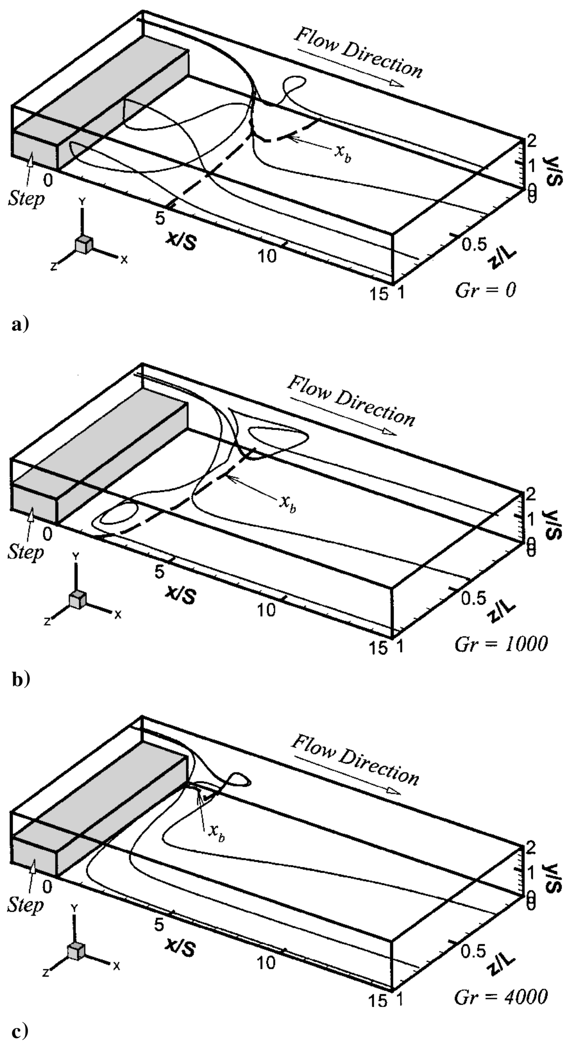

Fig. 3 Effects of Grashof number on flow patterns (streamlines) downstream from the step.

lines, x_u, and x_b, are different from each other for three-dimensional flow, but they are identical to each other for the two-dimensional flow, that is, at the center of a duct with large aspect ratio.

The results in Fig. 3 show that the primary recirculation region (region bounded by line x_b) decreases in size as the Grashof number increases and almost disappears for the large Grashof number of 4000. For that large Grashof number (Fig. 3c), the recirculation region is partially lifted away from the heated stepped wall by the buoyancy-induced streamwise flow. The streamlines in Fig. 3c near the heated wall and away from the sidewall are vented directly (without reversing their directions) to the main flow at the center of the duct. Similarly, the magnitude of the swirling flow in that region decreases as the Grashof number increases due to the associated increase of buoyancy-induced streamwise flow.

Limiting streamlines adjacent to the stepped wall ($y/S = 0.01$), the sidewall ($z/L = 0.01$), and the flat wall ($y/S = 1.99$) are presented in Fig. 4. Note that the flat wall is artificially raised away from its position to facilitate the viewing of the sidewall and stepped wall. The "source" point that appears in the limiting streamlines on the y plane adjacent to the stepped wall ($y/S = 0.01$ in Fig. 4) is the impingement region of the "jetlike" flow[5] that develops in the separating shear layer. This impingement region moves upstream toward the step as the Grashof number increases. Figure 4a also illustrates that, after the impingement of the jetlike flow, some streamlines are reflected sharply sideways toward the sidewall and upward toward the flat wall, to form a reverse flow region adjacent to the sidewall. The results in Fig. 4 also illustrate how some of these reflected streamlines impinge (source point) on the flat wall ($y/S = 1.99$), creating a reverse-flow region at the corner between the sidewall and the flat wall. The flow reverses its direction after it impinges on the flat wall and flows upstream toward the step due to the negative pressure gradient that is created from the sudden expansion. This flow reverses its direction again, thus forming reverse-flow regions adjacent to the sidewall and flat wall, and flows in the downstream direction. For low Grashof numbers, the reverse-flow region that develops at the upper corner of the sidewall is separated from the primary recirculation flow region, as shown in Fig. 4a, but these two

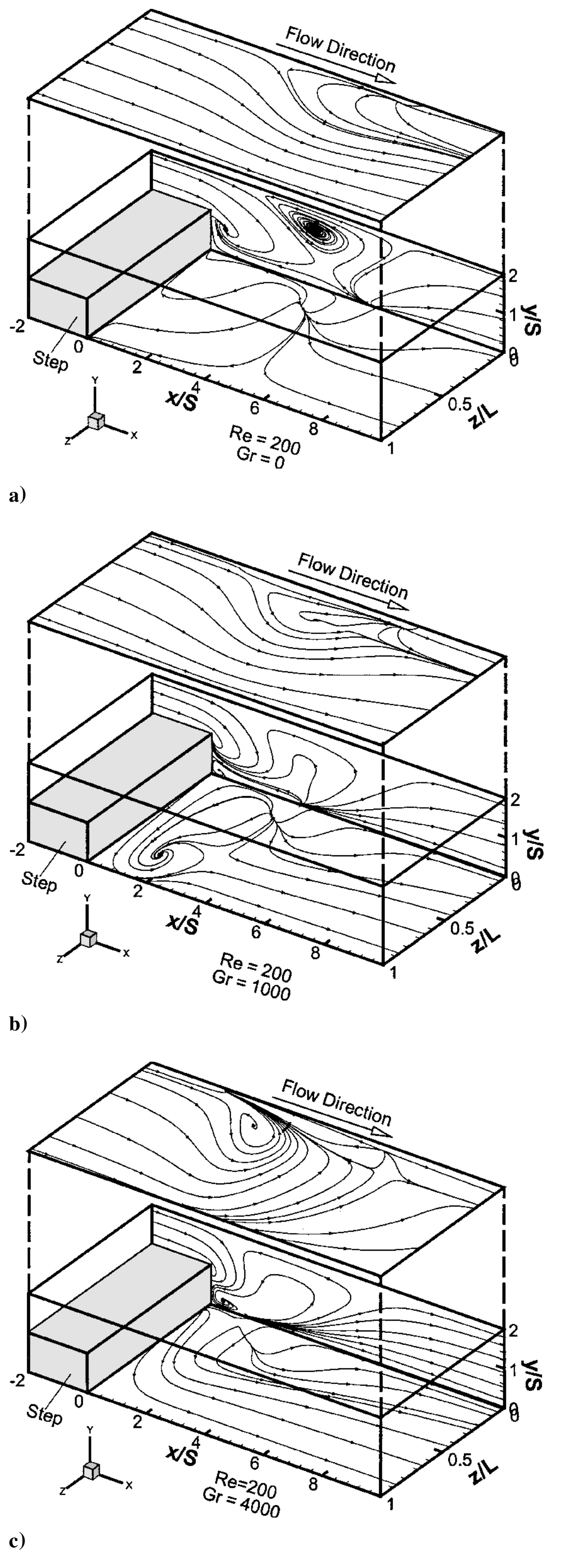

Fig. 4 Limiting streamlines adjacent to a) the stepped wall ($y/S = 0.01$), b) the sidewall ($z/L = 0.01$), and c) the flat wall ($y/S = 1.99$).

regions become connected for higher Grashof numbers as shown in Figs. 4b and 4c. The depth of the reverse-flow region in the spanwise direction extends to approximately 15% of the duct's half width for $Gr = 0$, but it extends to approximately 40% of the duct's half width at $Gr = 4000$.

Nusselt number [$Nu = q_w S/k(T_w - T_0)$, where T_w is wall temperature] distributions on the heated stepped wall are presented in Fig. 5. The jetlike flow impingement location and the location where the Nusselt number is at a maximum are also shown in Fig. 5, and they appear to develop in the same general region near the sidewall. The development of this peak in the Nusselt number distribution near the sidewall is directly due to the jetlike flow that develops in the separating shear layer and impinges in that region. The peak in this Nusselt number distribution moves upstream toward the step and closer to the sidewall as the Grashof number increases. The peak Nusselt number increases from 1.85 at $Gr = 0$ to 2.8 at $Gr = 4000$.

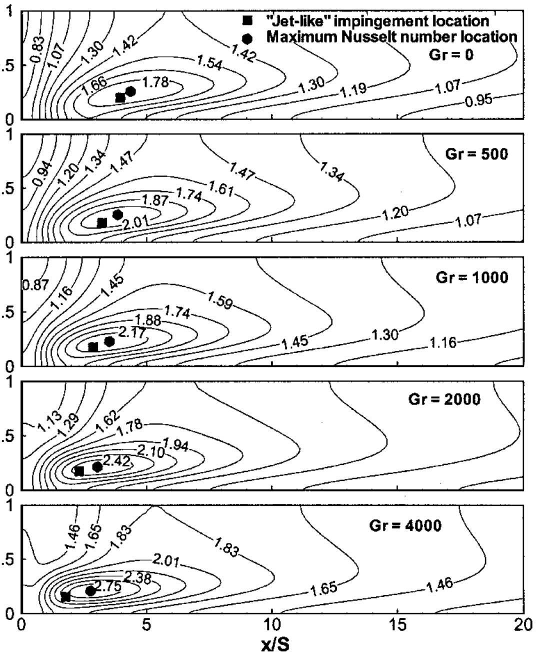

Fig. 5 Effects of Grashof number on the Nusselt number distribution ($y/S = 0$).

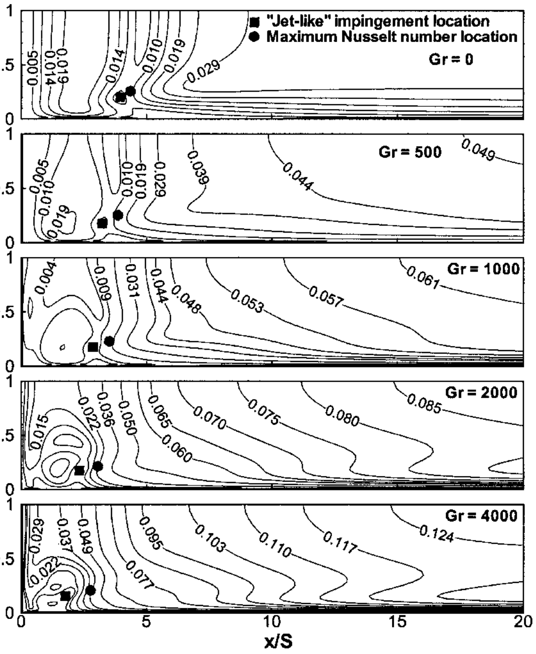

Fig. 6 Effects of Grashof number of the friction coefficient distribution ($y/S = 0$).

Distributions of the friction coefficient {$C_f = 2\tau_w/(\rho u_0^2)$, where shear stress $\tau_w = \mu\sqrt{[(\partial u/\partial y)^2 + (\partial w/\partial y)^2]}$} on the stepped wall are shown in Fig. 6. The two-dimensional behavior that occurs in the small region near the center of the duct for a zero Grashof number disappears as the Grashof number increases. The jetlike impingement location is a singular point with both zero streamwise velocity component u and zero spanwise velocity component w, and the friction coefficient at that point has its minimum value of zero. This location (impingement point) moves upstream and closer to the sidewall as the Grashof number increases. The location of the impingement point (zero friction coefficient) occurs upstream, closer to the step, from the location where the Nusselt number has its peak value as identified in Fig. 6.

Conclusions

Numerical simulations of three-dimensional, laminar, buoyancy-assisting mixed convection flow adjacent to a backward-facing step in a duct are presented to demonstrate the influence of the Grashof number on the flow behavior, distributions of the Nusselt number, distributions of the friction coefficient, and the reverse-flow regions that develop adjacent to the duct's walls. Increasing the Grashof number results in an increase in the Nusselt number and the size of the reverse-flow regions adjacent to the sidewall and the flat wall. On the other hand, the size of the primary recirculation flow region adjacent to the stepped wall decreases and detaches partially from the heated stepped wall as the Grashof number increases. The reverse-flow region that develops adjacent to the sidewall is not connected to the primary recirculation flow region for the cases of low Grashof number ($Gr = 0$ and 500) but becomes connected to that region at higher Grashof numbers. The locations where the Nusselt number is at a maximum and where the friction coefficient is at a minimum move upstream toward the step and closer to the sidewall as the Grashof number increases. The peak Nusselt number occurs downstream from the location where the friction coefficient is at a minimum (equal to zero) where the jetlike flow impinges onto the stepped wall.

Acknowledgment

This work was supported in part by the National Science Foundation under Grants CTS-9906746 and CTS-9818203.

References

[1] Armaly, B. F., Durst, F., Pereira, J. C. F., and Schonung, B., "Experimental and Theoretical Investigation of Backward-Facing Step Flow," *Journal of Fluid Mechanics*, Vol. 127, 1983, pp. 473–496.

[2] Simpson, R. L., "Aspects of Turbulent Boundary-Layer Separation," *Progress in Aerospace Sciences*, Vol. 32, No. 5, 1996, pp. 457–521.

[3] Eaton, J. K., and Johnson, J. P., "Review of Research on Subsonic Turbulent Flow Reattachment," *AIAA Journal*, Vol. 19, 1981, pp. 1093–1100.

[4] Pepper, D. W., and Carrington, D. B., "Convective Heat Transfer over a 3-D Backward Facing Step," *Proceedings of the ICHMT International Symposium on Advances in Computational Heat Transfer*, edited by G. de Vahl Davis and E. Leonardi, Begell House, New York, 1997, pp. 273–281.

[5] Armaly, B. F., Li, A., and Nie, J. H., "Three-Dimensional Forced Convection Flow Adjacent to Backward-Facing Step," *Journal of Thermophysics and Heat Transfer*, Vol. 16, No. 2, 2002, pp. 222–227.

[6] Iwai, H., Nakabe, K., Suzuki, K., and Matsubara, K., "The Effects of Duct Inclination Angle on Laminar Mixed Convective Flows over a Backward-Facing Step," *International Journal of Heat and Mass Transfer*, Vol. 43, No. 3, 2000, pp. 473–485.

[7] Li, A., and Armaly, B. F., "Mixed Convection Adjacent to 3-D Backward-Facing Step," *Proceedings of the ASME-IMECE Conference*, Vol. 366-2, American Society of Mechanical Engineers, Fairfield, NJ, 2000, pp. 51–58.

[8] Li, A., and Armaly, B. F., "Laminar Mixed Convection Adjacent to Three-Dimensional Backward-Facing Step," *Journal of Heat Transfer*, Vol. 124, No. 1, 2002, pp. 209–213.

[9] Patankar, S. V., "Numerical Heat Transfer and Fluid Flow," Hemisphere, New York, 1980, pp. 113–137.

[10] Shah, R. K., and London, A. L., "Laminar Forced Convection in Ducts," Academic Press, New York, 1978, pp. 196–198.

[11] Li, A., "Experimental and Numerical Study of Three-Dimensional Laminar Separated Flow Adjacent to Backward-Facing Step," Ph.D. Dissertation, Dept. of Mechanical and Aerospace Engineering and Engineering Mechanics, Univ. of Missouri, Rolla, MO, 2001.

Generalized Nonequilibrium Binary Scaling for Shock Standoff on Hypersonic Blunt Bodies

George R. Inger*
Iowa State University, Ames, Iowa 50011
and
Charlotte Higgins† and Richard Morgan‡
University of Queensland,
Brisbane, Queensland 4072, Australia

Introduction

The shock standoff distance δ_s in a blunt-body stagnation region (Fig. 1) is sensitive to the thermochemistry within the shock layer[1] and, hence, an important observable in hypervelocity test facilities.[2] Although numerical codes are available to predict δ_s, they are expensive for engineering parametric studies and do not yield physical insight and similitude laws needed for experimental design and data interpretation. On the other hand, existing analytical methods may not permit extension to include multitemperature ionization. The present paper examines a new analytical theory[3] of shock standoff with a nonequilibrium-dissociated shock layer to demonstrate a generalized binary scaling property for high-altitude hypervelocity flight simulation work.

Theoretical Formulation

We consider a blunt nose region at zero angle of attack under the following assumptions (Fig. 1): 1) The postshock static pressure is a known constant across the shock layer. 2) The tangential velocity component is of the form $U \approx \beta_S x$, where β_S is an appropriately defined known constant equal to the effective stagnation point velocity gradient reflecting the $U(y)$ variation. 3) Low Reynolds number viscous shock layer effects are negligible. For shock layer Reynolds numbers above 300 (pertaining to many applications), these assumptions are sufficient to model the main aerothermochemical aspects of the flow along the stagnation line $x \to 0$.

Regardless of the gas or its chemistry, continuity yields the normal velocity component V as

$$\rho(y)V(y) = -(1+J)\beta_S \int_0^y \rho \, \mathrm{d}y \tag{1}$$

where $J = 0$, 1 for two-dimensional or axisymmetric flow, respectively. When the density-stretched coordinate η is introduced,

$$\eta \equiv (1+J)\frac{\beta_S R_B}{U_\infty} \int_0^y \frac{\rho}{\rho_\infty} \mathrm{d}\left(\frac{y}{R_B}\right) \tag{2}$$

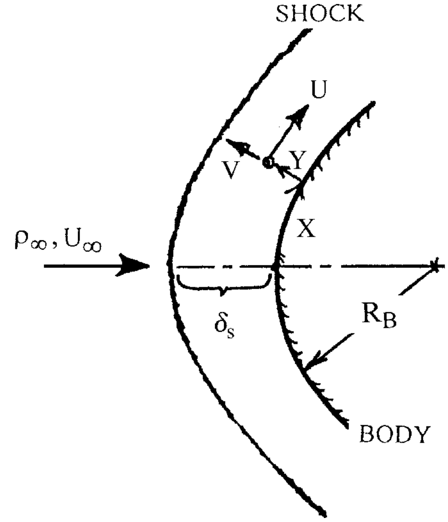

Fig. 1 Schematic of blunt-body stagnation shock layer.

Eq. (1) yields simply $\rho V = -\rho_\infty U_\infty \eta$. Because $\rho V = -\rho_\infty U_\infty$ behind the shock, $\eta = 1$ is, thus, the shock location regardless of the flow chemistry or dimensionality. The physical standoff distance $\delta_S = (y)_{\eta=1}$ by Eq. (2) is then

$$\frac{\delta_S}{R_B} = \left(\frac{U_\infty}{\beta_S R_B}\right)\left(\int_0^1 \left(\frac{\rho_\infty}{\rho}\right) \mathrm{d}\eta \Big/ (1+J)\right) \tag{3}$$

Equation (3) shows that once the density profile $\rho(\eta)$ is found using the species, energy, and state equations, one integration yields δ_s in a convenient nondimensional form.

For dissociation involving the net formation of an atom mass fraction α, we have along the stagnation line (neglecting diffusion) that $\rho V \, \mathrm{d}\alpha/\mathrm{d}y = \dot{w}_\alpha$, where $\dot{w}_\alpha$ is the net chemical rate of atom mass formation per unit volume. Then applying Eq. (2), we obtain the nondimensional equation

$$\eta \frac{\mathrm{d}\alpha}{\mathrm{d}\eta} = \frac{-(\dot{w}_\alpha/\rho)}{(1+J)\beta_S} = \frac{-(R_B U_\infty)(\dot{w}_\alpha \rho)}{(1+J)(\beta_S R_B/U_\infty)} \tag{4}$$

where both $\dot{w}_a/\rho$ and U_∞/R_B have the same units of reciprocal time.

Application to Dissociating Diatomic Gases

We now consider the specific case of a diatomic gas that undergoes the dissociation–recombination reaction

$$A_2 + M \underset{k_R}{\overset{k_D}{\rightleftarrows}} 2A + M \tag{5}$$

where M is a third body (molecule A_2 or atom A), k_D is the dissociation rate, and k_R is the recombination rate. The corresponding $\dot{w}_\alpha$ is formulated from the law of mass action combined with the principle of detailed balancing and the use of the usual mole-mass fraction relationship, giving Eq. (4) as[3]

$$\eta \frac{\mathrm{d}\alpha}{\mathrm{d}\eta} = \frac{-k_{DA2}\rho_\infty R_B U_\infty}{2(1+J)R_u T \lambda}\sqrt{\frac{(1-\varepsilon_F)}{2\varepsilon_F}}\left\{1 + \left[2\left(\frac{k_{DA}}{k_{DA2}}\right) - 1\right]\alpha\right\}$$
$$\times (1+\alpha)^{-1}\left\{(1-\alpha) - \left(\frac{4\rho R_{A2} T}{K_{\mathrm{eq}}}\right)\alpha^2\right\} \tag{6}$$

where $\varepsilon_F = \rho_\infty/\rho_F$, $k_{DA2} \equiv C T^N e^{-T_D/T}$, c_j are mass fractions $[c_A = \alpha,\ c_{A2} = (1-\alpha)]$, and $K_{\mathrm{eq}} = p_{\mathrm{ref}}(T/T_{\mathrm{ref}})^s e^{-(T_D/T)}$ in terms of the parameters p_{ref}, T_{ref}, s, and the dissociation temperature T_D.

The density ρ can be expressed in terms of α, the pressure p, and the mixture temperature T by the equation of state, which on use of Dalton's law becomes

$$p = \rho(R_u/M_{A2})T(1+\alpha) \tag{7}$$

Received 15 April 2002; revision received 28 June 2002; accepted for publication 28 June 2002.

[*] Professor, Department of Aerospace Engineering and Engineering Mechanics. Associate Fellow AIAA.

[†] Graduate Research Student, Centre for Hypersonics.

[‡] Professor, Centre for Hypersonics.